Acoustically-Mediated Intracellular Delivery

Shwathy Ramesan,[†] Amgad R. Rezk,[†] Chaitali Dekiwadia,[‡] Christina Cortez-Jugo,[¶] and Leslie Y. Yeo[*,†]

†*Micro/Nanophysics Research Laboratory, School of Engineering, RMIT University, Melbourne, VIC 3000, Australia*

‡*RMIT Microscopy and Microanalysis Facility, RMIT University, Melbourne, VIC 3000, Australia*

¶*ARC Centre of Excellence in Convergent Bio-Nano Science and Technology & Department of Chemical and Biomolecular Engineering, University of Melbourne, Parkville, VIC 3010, Australia*

E-mail: leslie.yeo@rmit.edu.au

Abstract

Recent breakthroughs in gene editing have necessitated practical *ex vivo* methods to rapidly and efficiently re-engineer patient-harvested cells. Many physical membrane-disruption or pore-forming techniques for intracellular delivery, however, result in poor cell viability, while most carrier-mediated techniques suffer from suboptimal endosomal escape and hence cytoplasmic or nuclear targeting. In this work, we show that short exposure of cells to high frequency (> 10 MHz) acoustic excitation facilitates temporal reorganisation of the lipid structure in the cell membrane that enhances translocation of gold nanoparticles and therapeutic molecules into the cell within just ten minutes. Due to its transient nature, rapid cell self-healing is observed, leading to high cellular viabilities ($> 97\%$). Moreover, the internalised cargo appears to be uniformly distributed throughout the cytosol, circumventing the need for strategies to facilitate endosomal escape. In the case of siRNA delivery, the method is seen to enhance gene silencing by over twofold, demonstrating its potential for enhancing therapeutic delivery into cells.

Keywords: intracellular delivery, acoustic irradiation, gene therapy, nanoparticle, siRNA

1 Introduction

The internalisation of therapeutic and imaging agents such as nucleic acids, peptides, proteins, nano-/molecular probes and nanoparticles, among others, into cells represents a crucial step in many of the next generation strategies currently being developed to diagnose and treat a variety of diseases (gene/cell therapy, gene editing, stem cell reprogramming or various theranostic approaches, as examples). The uptake of these exogenous materials, however, is severely restricted by the barrier imposed by the hydrophobic and apolar nature of the lipid bilayer that constitutes the cell membrane.[1] Considerable effort has therefore been dedicated to investigating the use of either physical (membrane-disruption-mediated) or biochemical (carrier-mediated) techniques to facilitate effective intracellular transport through the lipid bilayer.[2]

Physical methods for intracellular transport include electroporation, optoporation, sonoporation and microinjection,[3] in which physical forces are exploited to disrupt the structure of the cell membrane, particularly through the formation of pores. While this allows a wide range of submicron particulate matter to be delivered into the cell, a downside of a large proportion of these methods, however, lies in the damage inflicted on the cells during the poration process.[4] Electroporation, for example, which necessitates the application of high electric potentials across the cell membrane, often results in irreversible damage to the cell membrane, leading to a loss in homeostasis in the cell[5,6] and eventually apoptosis.[7–9] Sonoporation, on the other hand, primarily exploits the cavitation of microbubbles induced by sound waves near the cell membrane to enhance its permeabilisation. Given that the mechanical stress arising from a single oscillating microbubble alone has been found to be sufficient to cause profound membrane damage to the cell membrane,[10] it is not surprising that considerable cell death occurs due to the enormous stress the cells are subject to as a consequence of the intense shock waves and accompanying microjets generated during a cavitation event.[11–15] Additionally, cells have been shown to suffer from post-cavitation DNA damage due to the production of reactive oxygen species (ROS) as a result of free

radical formation during cavitation.[16–19] Consequently, cellular viabilities around 80%, and as low as 60%, are not uncommon with sonoporation.[20,21] The poor re-seeding viability and colony-forming ability of cells following exposure to ultrasonic radiation has also been documented.[22] Alternatively, ultrasonically-induced propulsion of asymmetric carriers in the form of nanowires have been exploited to drive molecular transport into cells, although we note the necessity for their functionalisation to endow them with a positive charge to aid entry through the lipid membrane.[23,24]

Biochemical carrier-mediated methods, on the other hand, which involve the use of viral or non-viral (e.g., polymers, peptides, vesicles or nanoparticles) vectors[25–27] to enhance cellular uptake via various endocytotic pathways offer an alternative method for intracellular delivery to the physical pore forming methods. They however often result in the trapping of high local concentrations of the cargo within the endosomal compartments of the cell. Bar their rare ($\lesssim 1\%$) ability to escape this endosomal recycling pathway[29–31] such that they are able to enter the cytoplasm where intracellular pathways exist to traffic them to the nucleus, if needed, the majority of the therapeutic cargo ends up in the lysosome,[32–35] where the highly acidic and enzyme-rich environment leads to their degradation.[36,37] A strategy that allows endosomal and lysosomal escape, or, better, avoidance of these organelles through a direct pathway into the cytosol is therefore necessary to enhance nuclear uptake and hence improve transfection efficiencies.

In this work, we explore a novel approach to enhance intracellular delivery of nanoparticles and macromolecules, whilst maintaining a high level of cell viability above 97%. This is first demonstrated with gold (Au) nanoparticles—which are widely used as nanocarriers,[38] for example in photodynamic therapy, given their inherent difficulty to be delivered into cells with currently available techniques,[39] especially if they are below 15 nm.[38] Additionally, we explore the uptake of fluorescently-labelled dextrans in order to observe the dependence of the internalisation on molecular size. To demonstrate therapeutic efficacy, we subsequently extend the technique to show the possibility of enhancing intracellular uptake and hence

transfection with small interfering RNA (siRNA), which has shown significant potential for the treatment of many diseases through RNA interference pathways by selectively suppressing or knocking out specific genes of interest. siRNA is however notoriously hard to deliver given that viral vectors typically used to enhance transfection efficiency can often induce an immune response, whereas non-viral carriers to which the siRNA is complexed are often unable to overcome intracellular barriers such as endosomal release.[40]

The method involves the exposure of cells to surface acoustic waves (SAWs)—high frequency (> 10 MHz) electromechanical Rayleigh waves, which, unlike their low frequency (< 1 MHz) bulk ultrasonic wave counterpart used in sonoporation, does not result in cavitation or excessive shear denaturation.[41] Importantly, unlike carrier-mediated methods or even some membrane-disruption-methods in which endocytosis constitutes the dominant internalisation mechanism,[42] we observe the majority of the nanoparticles and macromolecules to be uniformly distributed throughout the cytosol instead of accumulating within the endosomal and lysosomal compartments, thus enhancing the potential of the technique to increase nuclear targeting and hence transfection without necessitating complex strategies to effect endosomal/lysosomal release. As such, the method constitutes a promising *ex vivo* platform that allows rapid delivery of the desired therapeutic agent with the possibility for transient control to re-engineer target cells isolated from the blood or tissue of a patient in the laboratory, which is then infused back into the same patient[2]—an approach that is becoming increasingly attractive with recent breakthroughs in gene editing, including CRISPR–Cas9 (clustered regularly interspaced short palindromic repeats) and chimeric antigen receptor (CAR) T-cell therapy.[43]

2 Results and Discussion

2.1 Cellular nanoparticle uptake

When HEK293T cells were exposed to high frequency SAW irradiation (Fig. 1a) in the presence of fluorescein isothiocyanate (FITC) tagged Au nanoparticles for a specified duration (0.5, 2, 5, 7 or 10 mins), we observed from quantitative measurements of the internal cellular Au concentration with inductively coupled plasma mass spectrometry (ICP-MS) enhanced levels of nanoparticle uptake compared to the case in which nanoparticle internalisation occurred passively in the absence of an external force (Fig. 1b). In particular, the nanoparticle concentration was observed to increase with the exposure time, with an approximate two-fold enhancement in the uptake after 30 s to almost a six-fold increase within 10 mins. This is confirmed by flow cytometry (Fig. 1c), which shows a corresponding increase in side scatter due to the difference in the cell density with increasing uptake of the Au nanoparticles. Similar enhancement in the uptake were also observed with HeLa cells—see Fig. S1. Parenthetically, we note in Fig. 1c that slightly higher levels of side scatter were observed when the cells were exposed to the SAW in the absence of the nanoparticles compared to the unexposed control, indicating potential morphological changes to the cells when they are subjected to the acoustic irradiation, which we shall endeavour to elucidate subsequently in the context of a possible mechanism for the enhanced nanoparticle uptake upon SAW excitation.

In addition, the intracellular uptake of FITC-labelled dextran molecules of thee different molecular weights corresponding to approximate Stokes radii of 3.3, 6 and 10 nm, respectively, were also examined. In particular, an over two-fold increase in the internalisation of the lowest molecular weight dextran (20 kDa) was observed upon exposure to the SAW compared to the control, decreasing to a one and one half times increase for the largest molecular weight dextran (250 kDa) (Fig. 1d). In both the nanoparticle and dextran cases, the nonlinear departure from the slow and gradual linear change in uptake in the control

experiments highlights the significance of the effect of exposing the cells to the acoustic irradiation, and strongly suggests a distinctly different internalisation pathway to that if the nanoparticles or macromolecules were allowed to be taken up by the cells passively.

2.2 Post-exposure cell viability

Regardless of the exposure duration, we have found negligible effect of the SAW on the cell viability, as seen from the results of the MTT (3-(4,5-dimethylthiazol-2-yl)-2,5-diphenyltetrazolium bromide) assay in Fig. 2a (see also Fig. S1c), which is shown for the longest exposure duration of 10 mins; the cell viability was measured at three time points over 48 h post-exposure to the acoustic irradiation, with one measurement carried out immediately after the exposure to observe the immediate effect of the SAW on the cells (0 min). Over 97% of the cells were observed to remain viable post-treatment—significantly higher than the majority of other membrane-disruption-mediated delivery methods, particularly sonoporation, where typical viabilities generally range between 60% and 80% for similar cell lines, after treatment. This is because unlike conventional bulk ultrasound, whose excitation frequencies are generally in the Hz to kHz range, and never exceeding 1 MHz, the higher SAW frequencies and considerably lower powers (by approximately one to two orders of magnitude in comparison), not only significantly reduces heating (temperature increases no greater than approximately 2 °C were observed even after 10 mins of SAW exposure), but also completely suppresses any cavitation events that impose significant stresses on the cell membrane to the point at which pores are created. Moreover, at such high frequencies, the applied sound field, and the corresponding stress vector on the cell, reverses too quickly compared to the molecular relaxation time scale[41] such that macromolecules such as peptides and proteins are almost never degraded by the SAW, even at significantly larger powers than those employed here. Because of this, SAWs have widely been used for microfluidic trapping and manipulation of cells or microorganisms,[44–53] or even the nebulisation of nucleic acids, peptides, proteins and stem cells at much higher excitation powers than those employed in the present study with

little structural or functional degradation.[54–56]

Further confirmation of the post-exposure cell viability can be seen from close inspection of the confocal microscopy images of the cytoskeleton (actin network) and nuclei of the cells (Fig. 2b). Results from the Trypan blue exclusion assay to observe the long term proliferative ability of the cells[57] after they were trypsinised 24 h post exposure to the SAW and re-seeded showed an increase in the number of cells, revealing high ($> 90\%$) retention of the post-seeding efficiency, i.e., the majority of the cells remained adherent and viable (Fig. 2c; see also Fig. S1d). This is complemented by measurements of the mitochondrial membrane potential (MMP) (Fig. 2d) and the calcium flux levels (Fig. 2e) across the cell membrane, which play a vital role in stress-induced apoptosis. In the former, the negligible difference in the quantity of cell mitochondria that have been depolarised—an indicator of the deterioration in mitochondrial health that leads to cell apoptosis—between the control experiment (no SAW exposure) and cells exposed to the acoustic irradiation, as indicated by a decrease in the ratio of the red to green fluorescence intensity of cells stained with JC-1 dye (Fig. 2d), suggests that the acoustic irradiation does not affect the health of the cell membrane in a significant way. In support of this, the results from the Fura-2AM assay in Fig. 2e show an increase in the calcium flux into the cells immediately after exposure to the acoustic irradiation, although this returned to baseline values 10 mins after relaxation of the SAW excitation, suggesting fast resealing of the cell membrane and hence recovery of the cells following the high frequency acoustic forcing. A discussion on the underlying internalisation mechanism that allows for rapid healing of the membrane that explains the high post-exposure cellular viabilities will be presented below.

2.3 Cytosol distribution

Beyond enhanced levels in cellular uptake, we observe the internalised Au nanoparticles to be uniformly distributed throughout the cytosol when their uptake is mediated by the acoustic irradiation, as observed by the transmission electron microscopy (TEM) images in Fig. 3.

This was confirmed by the addition of calcein, a membrane-impermeant fluorophore, to the cells both in the presence and absence of SAW irradiation. In particular, addition of the calcein displayed a punctate appearance in the control cells showing endosomal/lysosomal entrapment, whereas the calcein appeared to be more evenly distributed throughout the cytosol in the presence of the SAW (Fig. S2a). These observations indicate the existence of an alternate mechanism for the internalisation of the nanoparticles under the acoustic forcing that does not follow the endocytotic pathway. Indeed, this is confirmed by the use of inhibitors to block the various receptor-mediated endocytosis pathways in which the nanoparticle internalisation experiments were repeated at 4 °C,[58] and in the presence of sodium azide (NaN_3), methyl-β-cyclodextrin and chlorpromazine.[59] In all of these cases, no discernible decrease in the nanoparticle uptake under SAW excitation was observed (Fig. S2b).

2.4 Internalisation mechanism

Given the plethora of evidence above that suggests endocytosis plays little or no role in the acoustically-mediated nanoparticle/macromolecule uptake, we now turn our attention to the possibility of membrane-disruption under the acoustic forcing. Unlike sonoporation, however, we do not observe any significant pore formation, as seen from the scanning electron microscopy (SEM) images in Fig. 4a. On the contrary, the presence of various submicron (500 nm in diameter) indentations were observed, although these were only apparent when the cells were fixed under 4% formaldehyde to 'freeze' their existence during SAW irradiation; in the absence of a fixative, or if the cells were fixed even immediately after the removal of the acoustic excitation, these submicron surface aberrations—which are considerably smaller than the typical 1–10 μm order pores that form under sonoporation[15,60,61]—were not observed even when the cells were imaged immediately after the acoustic excitation was relaxed (Fig. 4a). The transient nature of these nanoaberrations is substantiated by the results from the propidium iodide (PI) uptake experiments reported in Fig. 4b (see also Fig. S2c) where it can be seen that the PI uptake into the cell prior to acoustic excitation

(control) increases by almost 50% during SAW exposure, indicating a large diffusive flux through these transient surface aberrations, but rapidly decreases to approximately 20% immediately upon removal of the SAW (0 min) and approximately 10% ten mins after. The extremely short transient nature of the aberrations therefore further warrants significant distinction from the pores formed during conventional cell poration techniques—whether sonoporation, electroporation or other processes, since the sealing of the pores in these processes (and even smaller nanopores—for example, those that form under very high frequency pulsed ultrasound due to the high intensity of the short μs pulses, that commonly results in cell blebbing[62]) typically requires many minutes, if the membrane is able to reseal.[63] Such a long recovery procedure is clearly absent from the results for the MTT assay on cell viability in Fig. 2a, where it can be seen that no further cell recovery occurs with time (over many minutes) beyond an immediate healing of the aberrations upon cessation of the SAW irradiation.

The lack of pore formation is perhaps unsurprising given the absence of cavitation events required to drive pore formation at the SAW excitation frequencies and powers used, let alone even at much higher powers when nebulisation ensues.[64] Rather, we postulate that the high frequency yet continuously distributed low amplitude (in contrast to short but very intense high frequency focussed pulses[62]) sound wave excitation is enough to disorder the lipid structure comprising the cell membrane to sufficiently induce transient gaps between the lipid molecules. These gaps are large enough to facilitate diffusional translocation of the nanoparticles or macromolecules but considerably smaller than the physical pores created by conventional poration methods. The Fourier Transform Infrared (FTIR) spectrum shown in Fig. 4c indeed indicates a change in the organisation of the lipid structure upon acoustic irradiation of the cells, thereby altering the fluidity of the membrane lipids due to the shift from their ordered to disordered state,[65–68] which, in turn, increases the permeability of the cell membrane. We note that a similar mechanism that facilitated nanoparticle/macromolecular diffusion into cells was reported when they were subjected to shear and compressional forces

as the cells were forced through a microfluidic constriction,[39] which acted to disrupt the membrane lipid structure. In addition to facilitating nanoparticle distribution throughout the cytosol, consistent with that observed in the present work, the cells were also observed to self-repair within 30 secs (as observed in the PI uptake), compared to the much longer time scales (several minutes or tens of minutes) typically associated with pore recovery.[62]

Our hypothesis is not without precedent given that mechanically oscillating a cell even at sub-kHz frequencies have been observed to disorder the cell membrane to increase its permeability.[69] In addition, SAWs at comparable frequencies to that employed in the present work have been shown to induce structural alterations to the cell membrane lipid structure that involves changes in the tilt of the lipid headgroups from its equilibrium state.[70] Interestingly, we observe in Fig. 4c a considerable shift in the absorption band at 2917 cm^{-1} associated with the anti-symmetric vibrational stretching of the olefinic (CH_2) group in the hydrocarbon tail of the lipid to 2922 cm^{-1}, indicating a higher degree of acyl chain unsaturation and hence an increase in the membrane fluidity due to exposure of the cell to the SAW irradiation. After 10 mins, however, we observe a shift in the vibrational stretching frequency back to its original state, indicating fast self-restoration of the lipid structure upon relaxation of the acoustic excitation.

2.5 Gene delivery

Figure 5a (see also Fig. S4) shows that it is possible to approximately double the efficiency in the uptake of Cy3-labelled siRNA targeting the glyceraldehyde 3-phosphate dehydrogenase (GAPDH) gene in HeLa cells with the application of the SAW irradiation compared to that of the unexposed control. As with the internalisation of Au nanoparticles, we also observed the siRNA delivered into the cells with the SAW irradiation to be distributed through the cytosol, including some in the lysosomes (Fig. 6). This increase in internalisation efficiency and the ability to distribute the siRNA throughout the cytosol, thus avoiding endosomal recycling, then translates into a marked increase in the efficiency of silencing GAPDH, as

observed by the twofold decrease in the expression of GAPDH mRNA levels measured using real time quantitative reverse transcription polymerase chain reaction (qRT-PCR) compared to equivalent samples that were not exposed to the SAW (Fig. 5b). These results are also consistent with the approximate twofold knockdown in the GAPDH protein levels observed in Fig. 5c 48 and 72 h post-SAW irradiation compared to the unexposed samples.

3 Conclusion

In summary, we have demonstrated a novel technique that allows rapid and efficient internalisation of therapeutic agents into cells using high frequency surface acoustic waves. Unlike conventional sonoporation, which operates at much higher powers and lower frequencies, the technique does not rely on cavitation to induce poration, which can be to the detriment of the cells. Instead, the acoustic excitation induces resonant modes along the cell membrane that transiently reorganises its lipid structure to facilitate rapid translocation of the nanoparticles or macromolecules through the cell membrane. The membrane however reseals almost immediately upon removal of the excitation such that the viability of the cell is highly preserved. Moreover, in contrast to biochemical carrier-mediated methods which rely on endocytotic internalisation pathways, the therapeutic cargo is distributed throughout the cytosol as opposed to accumulating mostly in the endosomes. By reducing the chance of degradation in the endosomal compartments, the cargo then has a better chance of being trafficked to the nucleus or to the desired intracellular target site, therefore leading to higher transfection efficiencies. Given the low-cost ($< \$10$/device) chipscale nature of the platform, it is possible to employ a large number of these devices in parallel to facilitate high throughput *ex vivo* intercellular delivery, particularly for next generation macromolecular and gene therapeutics.

4 Materials and Methods

4.1 Materials

Dulbecco's Modified Eagle Medium (D-MEM), Opti-MEM® Reduced Serum Media, RNase-free water, nuclease-free water, fetal bovine serum (FBS), Gibco penicillin–streptomycin, Dulbecco's phosphate buffered saline (D-PBS), calcein AM, propidium iodide (PI), 0.4% Trypan Blue Solution, LysoTracker® Red DND-99, LysoTracker® Green DND-26, MitoTracker® Green FM, MitoTracker® Deep Red FM, Alexa Fluor® 594 phalloidin, Hoechst 33342 nuclear staining dye, Fura-2 AM, JC-1 Dye, Vybrant® MTT Cell Proliferation Assay Kit, Nunc™ Lab-Tek® CC2 chamber slide system, Lipofectamine® 2000 Transfection Reagent, RNase AWAY® Surface Decontaminant, Silencer® Cy3™-Labeled GAPDH siRNA, Silencer® Negative Control siRNA, Human GAPDH TaqMan® Primer, Human β-actin RT-PCR primer, UltraPure™ Agarose, UltraPure™ 10X TBE Buffer, SYBR® Safe DNA Gel Stain, DNA Gel Loading Dye, KDalert™ GAPDH Assay Kit and TRIzol® reagent were obtained from Life Technologies Pty. Ltd. (Mulgrave, VIC, Australia). Calcium fluoride windows (5 mm) for the FTIR measurements were obtained from Edmund Optics Pte. Ltd. (Singapore). The OneStep RT-PCR Kit was acquired from Qiagen Pty. Ltd. (Chadstone, VIC, Australia). Unless otherwise stated, all other chemicals were obtained from Sigma-Aldrich Pty. Ltd. (Castle Hill, NSW, Australia).

4.2 SAW devices

The experimental setup is as illustrated in Fig. 1a. The SAW devices consisted of 127.86° Y–X rotated lithium niobate ($LiNbO_3$) single crystal piezoelectric substrates (Roditi Ltd., London, UK) on which 40 alternating finger pairs of straight interdigitated transducer (IDT) electrodes comprising a 66 nm layer of aluminium atop a 33 nm chromium layer were photolithographically patterned. The width and the gap of the IDT fingers determines the wavelength and hence its resonant frequency, which, in the present case, is designed to be

398 μm and 10 MHz, respectively. Application of an alternating electrical signal to the IDTs at this resonant frequency with the aid of a signal generator (SML01, Rhode & Schwarz Pty. Ltd., North Ryde, NSW, Australia) and amplifier (10W1000C, Amplifier Research, Souderton, PA, USA) then launches a SAW that propagates as a Rayleigh wave along the surface of the substrate. In the present work, we maintain a constant input power of 2 W to the device across all experiments. To couple the acoustic energy to the cells, the device was mounted beneath a glass-bottomed 8-well chamber slide containing the cells and media. A thin layer of silicone oil with viscosity 45-55 cP and density 0.963 g/ml at 25 °C was applied between the device and well plate to aid the coupling of the acoustic energy into the wells[71,72] and to minimise the acoustic impedance mismatch.

4.3 Synthesis and characterisation of Au nanoparticles

Spherical Au nanoparticles were utilised as model particles to study the internalisation dynamics given their difficulty to be internalised in cells,[39] particularly when their dimensions are below 10 nm.[38] These nanoparticles have been employed in various cell lines owing to their non-toxicity, ease-of-synthesis and well-defined characterisation techniques. The nanoparticles were synthesised using standard solution techniques and stabilised with citrate capping with no further surface modification. Briefly, aurochloric acid ($HAuCl_4$) and sodium citrate were combined at 60 °C and sodium borohydrate employed as the reducing agent to form uniform, spherical nanoparticles. The synthesised nanoparticles were further concentrated two-fold using a rotavaporator for 6 h at 50 °C to yield a final concentration of 40 μg/ml. Dynamic light scattering (DLS; Zetasizer Nano S, Malvern Instruments Ltd., Malvern, UK) with an emission wavelength of 658 nm revealed a mean nanoparticle hydrodynamic diameter of 10 ± 5 nm and a zeta potential of -25 ± 3 mV (negative due to the presence of the citrate molecules). The nanoparticles were further characterised using TEM (1010, JEOL Inc., Peabody, MA, USA), which verified their spherical shape and 10 nm size range, free from aggregation (Fig. S3 inset), and UV-Vis spectrophotometry (V-570, Jasco Inc., Easton,

MD, USA), which showed a signature peak at 519 nm typical of the Au nanoparticles.

Additionally, fluorescently-labelled nanoparticles were synthesised for use with a confocal microscope (N-STORM Super-Resolution Microscope, Nikon Corp., Tokyo, Japan) to investigate the co-localisation of nanoparticles in order to examine their distribution within and external to the organelles. Specifically, fluorophores were conjugated to the citrate capped Au nanoparticles by adding FITC to yield a final concentration of 50 μM. The stock solution was then centrifuged at 6000 rpm for 20 mins at 4 °C after allowing the FITC to conjugate with the nanoparticles for 12 h. The pellet was then washed thrice with deionised water to remove unbound FITC molecules and redispersed in fresh water ready for use. When the nanoparticles were added to the cells, utmost care was taken to conduct all the experiments in serum-free media to avoid the formation of a protein corona around the nanoparticles, which may alter the mechanism of their internalisation within the cells.

4.4 Cell culture and acoustic irradiation

Human embryonic kidney cells (HEK 293-T; Invitrogen™, ThermoFisher Scientific Inc., Waltham, MA, USA) and cervical cancer cells (HeLa; Invitrogen™, ThermoFisher Scientific Inc., Waltham, MA, USA), were cultured in DMEM supplemented with 10% FBS and 1% penicillin–streptomycin (100 units/ml) in a humidified incubator maintained at 37 °C and 5% CO_2. The cells were grown in a standard T25 flask until they reached 80–90% confluency. They were then detached using 0.25% trypsin–EDTA 24 h prior to the experiments and re-seeded in 8-well plates at a density of 200,000/ml 24 h prior to the experiments. The cells in the well plate were then irradiated with the SAW through the silicone oil coupling layer, as described above, for the stipulated duration. Following cessation of the acoustic field, the cells and media were immediately removed for further analysis.

4.5 ICP-MS

0, 5, 10, 50 and 100 ppb nanoparticle concentration standards were first prepared in 3% hydrochloric acid (HCl) for the elemental Au analysis using ICP-MS (7700x and ASX-520 autosampler, Agilent Technologies, Santa Clara, CA, USA). Specifically, 2×10^5 cells in the glass-bottom well plates in the same concentration of Au nanoparticles both with and without exposure to SAW irradiation for the specified duration were washed thrice with fresh PBS to remove the nanoparticles that were bound to the surface. The cells were then trypsinized and collected in 1.5 ml centrifuge tubes to which 0.5 ml of concentrated HCl (30%) was added and heated to 70 °C for 30 mins. The samples were further reconstituted with double-distilled water to obtain a final concentration of 3% HCl for the ICP-MS analysis to determine the amount of Au in the cells.

4.6 Flow cytometry

Flow cytometry (BD C_6, Accuri, BD Biosciences, San Jose, CA, USA) was carried out using a 488 nm laser to assess nanoparticle uptake by observing the change in the mean side scatter (SSC).[73] Following SAW irradiation and prior to the analysis, the cells were left in the incubator at 37 °C for 4 h along with the control samples. The samples were then washed thrice with PBS, followed by trypsinisation, centrifugation at 1200 rpm for 5 mins and finally reconstitution into 0.5 ml of fresh PBS. Gating was carried out on the basis of untreated cells from which the SSC can be determined.

4.7 Cell viability, proliferation, permeability, calcium flux and membrane potential measurements

Cytotoxic effects induced by the presence of the nanoparticles and exposure to acoustic irradiation were evaluated using a MTT proliferation assay. Briefly, the cells were washed with PBS immediately after the experiments following which 3-(4,5-dimethylthiazolyl-2)-

2,5-diphenyltetrazolium bromide (MTT) solution at a final concentration of 0.5 mg/ml in serum-free medium was added to each well. This was also repeated for two further samples which were left undisturbed in the incubator at 37 °C after the experiments for 24 and 48 h to observe long-term cytotoxicity effects. In each case, the reduction of MTT by cells which are still metabolically active due to the dehydrogenase enzyme results in the formation of purple formazan crystals that is then dissolved in dimethylsulfoxide (DMSO), whose absorption is measured at 570 nm using a spectrophotometric plate reader (SpectraMax® Paradigm Multi-Mode Plate Reader, Molecular Devices LLC, Sunnyvale, CA, USA) and normalised with respect to the absorbance of the control with neither the presence of the nanoparticles nor the exposure to the acoustic waves.

A Trypan blue exclusion assay was performed to assess the re-seeding efficiency of the cells. We first added the Trypan blue solution (0.4%) to trypsinised cells immediately after SAW exposure on day 1. The cells were then detached using 0.25% trypsin–EDTA and counted with a standard haemocytometer by mixing the cell suspension and the Trypan blue solution in equal ratio to obtain the immediate post-exposure cell viability. The same experiments were repeated on day 3 to observe the longer term effect of the SAW irradiation on cell proliferation and attachment.

Given that leaky cell membranes—either because the cells have undergone apoptosis, or, in the present case, due to the permeabilisation of the membrane—are permeable to PI, we examined the PI levels in the cell to provide us with an indication of the transient dynamics associated with reorganisation of the lipid structure. PI was added to both untreated (control) and treated (SAW irradiated) cells for 5 mins followed by thrice washing in PBS. The fluorescence intensity of the cells was then analysed via the flow cytometry FL2-A channel (Fig. S2c). Additionally, the calcium flux into the cells was measured using Fura-2AM—a membrane permeable ratiometric calcium ion indicator that emits at fluorescent wavelengths under UV excitation—via the plate reader.

To measure the MMP, a stock solution of JC-1 dye, which is a cationic dye that accu-

mulates in energised mitochondria, was prepared by dissolving 2 mg/ml in DMSO in 30 µl aliquots and stored at −20°C. Following the experiments, the JC-1 aliquot was reconstituted to a final concentration of 1 µg/ml in PBS, and 500 µl was added to each well, which was then incubated at 37 °C for 20 mins. The structural anomaly of the mitochondrial membrane can then be inferred from its potential state by examining the relative fluorescence between its green monomeric (depolarised) form at 585 ± 15 nm via excitation at 514 nm with that of its red aggregated (hyperpolarised) form at 590 ± 17.5 nm through excitation at 529 nm, evaluated using a microscope (ZOE™ Fluorescent Cell Imager, Bio-Rad Laboratories Inc., Hercules, CA, USA) at 20X magnification.

4.8 Microscopy

The cells were fixed with 1% (w/v) osmium tetroxide and 1.5% (w/v) potassium ferrocyanide for an hour at room temperature, followed by three cycles of rinsing in distilled water and centrifugation at $800 \times g$ for 5 mins. The cells were further dehydrated with increasing gradients (50% to 100%) of ethanol for 15 mins for each step. Following ethanol treatment, absolute acetone was added twice to the cells for 30 mins to completely dehydrate the cells, after which they were infiltrated twice with equal parts of acetone to Spurr's resin. As a final step, the cells were infiltrated twice with 100% resin under vacuum conditions. Finally, the resin containing the cells was incubated at 70 °C for 24 h. Ultrathin sections of the cells of 90 nm thicknesses were then sectioned using a diamond knife (Diatome AG, Nidau, Switzerland) on an ultramicrotome (Ultracut UCT, Leica Microsystems Pty. Ltd., Macquarie Park, NSW, Australia) and post-stained for imaging under TEM (JEM 1010, JEOL Inc., Peabody, MA, USA) at 80 kV.

For SEM (FEI Scios™ DualBeam™, ThermoFisher Scientific Inc., Waltham, MA, USA), the samples were immediately fixed with 2.5% glutaraldehyde for 60 mins at room temperature, after which they were washed thrice with 0.1 M sodium cacodylate buffer and dehydrated with the same ethanol wash steps described above. The samples were then left

to dry in air overnight to dehydrate the samples completely, after which they were sputter coated with carbon prior to imaging. For confocal microscopy (N-STORM Super-Resolution Microscope, Nikon Corp., Tokyo, Japan), the samples were stained with the respective organelle stains (Lysotracker®/MitoTracker®) for 20 mins at 37 °C followed by nuclear staining (5 μM) for 5 mins. The samples were finally washed thrice and loaded with fresh PBS before imaging. To stain the cytoskeleton, 100 μl (1:40 dilution in staining buffer) of phalloidin was added to the wells for 2 h at room temperature. Calcein staining for the endosomal entrapment experiments, on the other hand, was carried out by adding 100 μg/ml of calcein AM to the cells in the presence of the SAW over the specified duration. The cells were then further incubated for 2 h and rinsed four times with PBS to remove excess and non-internalised calcein prior to image acquisition via fluorescence microscopy (ZOE™ Fluorescent Cell Imager, Bio-Rad Laboratories Inc., Hercules, CA, USA) at 20× magnification. The control samples were maintained at the same conditions as that of the SAW exposed samples, but in the absence of the SAW irradiation.

4.9 Gene expression

Prior to the transfection experiments, cells were grown to 60% confluency on glass-bottomed 8-well chamber plates in DMEM medium with 10% FBS, 1% pencillin–streptomycin and 5% CO_2 at 37 °C. All transfection experiments were carried out 24 h post-seeding. The media was removed and the samples were washed twice in sterile PBS before the addition of the transfection reagents. siRNA and Lipofectamine® (where applicable) were mixed at a 1:5 molar ratio to a final working concentration of 20 nM siRNA and 1 μl Lipofectamine® per 500 μl Opti-MEM® reduced serum media in RNase- and nuclease-free distilled water, followed by a further pre-incubation step for 15 mins at room temperature to form the siRNA–Lipofectamine® complex. The transfection solution was added to both the SAW and control samples at the same time and left in the incubator for 24 h prior to the replacement of transfection mixture in the wells with fresh serum-free media. For the mock controls, the cells

were left in serum-free media, while control samples contained siRNA and Lipofectamine® diluted in Opti-MEM® reduced serum media at a 1:5 ratio. Scrambled siRNA comprising random nucleotide sequences were used as sham controls to consider off-target silencing, if any. The samples exposed to the SAW were treated under the same conditions as that of the control samples and subjected to 5 mins of the acoustic irradiation. The samples were then left undisturbed for 72 h before being analysed using quantitative RT-PCR (CFX96 Touch™ Real-Time PCR Detection System, Bio-Rad Laboratories Inc., Hercules, CA, USA) as well as with the Qiagen OneStep PCR Kit according to the manufacturer's instructions, with β-actin as the reference gene. The kit, comprising 5X RT-PCR buffer, 5X Q-solution, 10 mM dNTP mix, one step RT-PCR enzyme mix, was added to 250 ng of the RNA that was obtained to make a final reaction volume of 20 µl. This was then added to a 96-well PCR plate before being subjected to 40 PCR thermocycles (50 °C for 30 mins, 95 °C for 15 mins, 94 °C for 0.5 mins, 50 °C for 0.5 mins, 72 °C for 1 min and a final extension at 72 °C for 10 mins).

Total RNA was extracted from the cells using ethanol, isopropanol and TRIzol® and was diluted to 250 ng per reaction for each sample after measuring the amount and quality of RNA extracted using a spectrophotometer (OPTIZEN Nano Q, Mecasys Co. Ltd., Daejeon, Korea) in which the A260/A280 absorbance ratio was maintained at a range of 1.9–2.2; samples outside this prescribed range were discarded. Amplified DNA samples were further processed using gel electrophoresis. Briefly, 1.5% agarose gel was prepared in 0.5X TBE buffer and mixed with SYBR® Safe DNA Gel Stain. The mixture was then allowed to set for 30 mins in a gel tray, following which we added the DNA sample from the aforementioned PCR analysis to which DNA loading dye (1X) was added. Gels were run at 80 V for 45 mins prior to imaging (ChemiDoc™ XRS+, Bio-Rad Laboratories Inc., Hercules, CA, USA).

4.10 Statistical significance

Data presented in this study are expressed as the mean ± the standard error of replicate measurements (minimum of six). They were then analysed using a two-tailed, unpaired Student's t-test, where applicable.

References

(1) Barua, S.; Mitragotri, S. Challenges Associated with Penetration of Nanoparticles Across Cell and Tissue Barriers: A Review of Current Status and Future Prospects. *Nano Today* **9**, 223–243 (2014).

(2) Stewart, M. P.; Sharei, A.; Ding, X.; Sahay, G.; Langer, R.; Jensen, K. F. *In Vitro* and *Ex Vivo* Strategies for Intracellular Delivery. *Nature* **538**, 183–192 (2016).

(3) Mehier-Humbert, S.; Guy, R. H. Physical Methods for Gene Transfer: Improving the Kinetics of Gene Delivery into Cells. *Adv. Drug Deliv. Rev.* **57**, 733–753 (2005).

(4) Agarwal, J.; Walsh, A.; Lee, R. C. Multimodal Strategies for Resuscitating Injured Cells. *Ann. N. Y. Acad. Sci.* **1066**, 295–309 (2006).

(5) Rubinsky, B. Irreversible Electroporation in Medicine. *Technol. Cancer Res. Treat.* **6**, 255–259 (2007).

(6) Lee, E. W.; Chen, C.; Prieto, V. E.; Dry, S. M.; Loh, C. T.; Kee, S. T.; Advanced Hepatic Ablation Technique for Creating Complete Cell Death: Irreversible Electroporation. *Radiology* **255**, 426–433 (2010).

(7) Li, S. Electroporation Gene Therapy: New Developments *In Vivo* and *In Vitro*. *Curr. Gene Ther.* **4**, 309–316 (2004).

(8) Geng, T.; Lu, C. Microfluidic Electroporation for Cellular Analysis and Delivery. *Lab Chip* **13**, 3803–3821 (2013).

(9) Yarmush, M. L.; Golberg, A.; Serša, G.; Kotnik, T.; Miklavčič, D. Electroporation-Based Technologies for Medicine: Principles, Applications, and Challenges. *Annu. Rev. Biomed. Eng.* **16**, 295-320 (2014).

(10) Marmottant, P.; Hilgenfeldt, S. Controlled Vesicle Deformation and Lysis by Single Oscillating Bubbles. *Nature* **423**, 153–156 (2003).

(11) Abdollahi, A.; Domhan, S.; Jenne, J. W.; Hallaj, M.; Dell'aqua, G.; Mueckenthaler, M.; Richter, A.; Martin, H.; Debus, J.; Ansorge, W.; Hynynen, K.; Huber, P. E. Apoptosis Signals in Lymphoblasts Induced by Focused Ultrasound. *FASEB J.* **18**, 1413–1414 (2004).

(12) Mehier-Humbert, S.; Bettinger, T.; Yan, F.; Guy, R. H. Plasma Membrane Poration Induced by Ultrasound Exposure: Implication for Drug Delivery. *J. Control. Release* **104**, 213–222 (2005).

(13) Mehier-Humbert, S.; Bettinger, T.; Yan, F.; Guy, R. H. Ultrasound-Mediated Gene Delivery: Kinetics of Plasmid Internalization and Gene Expression. *J. Control. Release* **104**, 203–211 (2005).

(14) Kosheleva, O. K.; Lai, T.-C.; Chen, N. G.; Hsiao, M.; Chen, C.-H. Selective Killing of Cancer Cells by Nanoparticle-Assisted Ultrasound. *J. Nanobiotechnol.* **14**, 46 (2016).

(15) Prentice, P.; Cuschieri, A.; Dholakia, K.; Prausnitz, M.; Campbell, P. Membrane Disruption by Optically Controlled Microbubble Cavitation. *Nat. Phys.* **1**, 107–110 (2005).

(16) Kondo, T.; Fukushima, Y.; Kon, H.; Riesz, P. Effect of Shear Stress and Free Radicals Induced by Ultrasound on Erythocytes. *Arch. Biochem. Biophys.* **269**, 381–389 (1989).

(17) Honda, H.; Kondo, T.; Zhao, Q.-L.; Feril, L. B.; Kitagawa, H. Role of Intracellular Calcium Ions and Reactive Oxygen Species in Apoptosis Induced by Ultrasound. *Ultrasound Med. Biol.* **30**, 683–692 (2004).

(18) Milowska, K.; Gabryelak, T. Reactive Oxygen Species and DNA Damage After Ultrasound Exposure. *Biomol. Eng.* **24**, 263–267 (2007).

(19) Furusawa, Y.; Fujiwara, Y.; Campbell, P.; Zhao, Q.-L.; Ogawa, R.; Hassan, M. A.; Tabuchi, Y.; Takasaki, I.; Takahashi, A.; Kondo, T. DNA Double-Strand Breaks In-

duced by Cavitational Mechanical Effects of Ultrasound in Cancer Cell Lines. *PLoS One* **7**, e29012 (2012).

(20) Qiu, Y.; Zhang, C.; Tu, J.; Zhang, D. Microbubble-Induced Sonoporation Involved in Ultrasound-Mediated DNA Transfection *In Vitro* at Low Acoustic Pressures. *J. Biomech.* **45**, 1339–1345 (2012).

(21) Feril Jr., L. B.; Kondo, T.; Zhao, Q.-L.; Ogawa, R.; Tachibana, K.; Kudo, N.; Fujimoto, S.; Nakamura, S. Enhancement of Ultrasound-Induced Apoptosis and Cell Lysis by Echo-Contrast Agents. *Ultrasound Med. Biol.* **29**, 331–337 (2003).

(22) Kaufman, G. E.; Miller, M. W.; Griffiths, T. D.; Ciaravino, V.; Carstensen, E. L. Lysis and Viability of Cultured Mammalian Cells Exposed to 1 MHz Ultrasound. *Ultrasound Med. Biol.* **3**, 21–25 (1977).

(23) Esteban-Fernández de Ávila, B.; Angell, C.; Soto, F.; Lopez-Ramirez, M. A.; Báez, D.; Xie, S.; Wang, J.; Chen, Y. Acoustically Propelled Nanomotors for Intracellular siRNA Delivery. *ACS Nano* **15**, 4997–5005 (2016).

(24) Hansen-Bruhn, M.; Esteban-Fernández de Ávila, B.; Beltrán-Gastélum, M.; Zhao, J.; Ramírez-Herrera, D. E.; Angsantikul, P.; Vesterager Gothelf, K.; Zhang, L.; Wang, J. Active Intracellular Delivery of Cas9-sgRNA Complex Using Ultrasound-Propelled Nanomotors. *Angew. Chem. Int. Ed.* DOI: 10.1002/ange.201713082 (2018).

(25) Yin, H.; Kanasty, R. L.; Eltoukhy, A. A.; Vegas, A. J.; Dorkin, J. R.; Anderson, D. G. Non-Viral Vectors for Gene-Based Therapy. *Nat. Rev. Genet.* **15**, 541–555 (2014).

(26) Mingozzi, F.; High,K. A. Therapeutic *In Vivo* Gene Transfer for Genetic Disease Using AAV: Progress and Challenges. *Nat. Rev. Genet.* **12**, 341–355 (2011).

(27) Kotterman, M. A.; Schaffer, D. V. Engineering Adeno-Associated Viruses for Clinical Gene Therapy. *Nat. Rev. Genet.* **15**, 445–451 (2014).

(28) Gould, G. W.; Lippincott-Schwartz, J. New Roles for Endosomes: From Vesicular Carriers to Multi-Purpose Platforms. *Nat. Rev. Mol. Cell Biol.* **10**, 287–292 (2009).

(29) Varkouhi, A. K.; Scholte, M.; Storm, G.; Haisma, H. J. Endosomal Escape Pathways for Delivery of Biologicals. *J. Control. Release* **151**, 220–228 (2011).

(30) Rejman, J.; Bragonzi, A.; Conese, M. Role of Clathin and Caveolae-Mediated Endocytosis in Gene Transfer Mediated by Lipo-and Polyplexes. *Mol. Ther.* **12**, 468–474 (2005).

(31) Gilleron, J.; Querbes, W.; Zeigerer, A.; Borodovsky, A.; Marsico, G.; Schubert, U.; Manygoats, K.; Seifert, S.; Andree, C.; Stöter, M.; Epstein-Barash, H.; Zhang, L.; Koteliansky, V.; Fitzgerald, K.; Fava, E.; Bickle, M.; Kalaidzidis, Y.; Akinc, A.; Maier, M.; Zerial, M. Image-Based Analysis of Lipid Nanoparticle-Mediated siRNA Delivery, Intracellular Trafficking and Endosomal Escape. *Nat. Biotechnol.* **31**, 638–646 (2013).

(32) Suh, J.; An, Y.; Tang, B. C.; Dempsey, C.; Huang, F.; Hanes, J. Real-Time Gene Delivery Vector Tracking in the Endo-Lysosomal Pathway of Live Cells. *Microsc. Res. Tech.* **75**, 691–697 (2012).

(33) Lu, J. J.; Langer, R.; Chen, J. A Novel Mechanism is Involved in Cationic Lipid-Mediated Functional siRNA Delivery. *Mol. Pharm.* **6**, 763–771 (2009).

(34) Nguyen, J.; Szoka, F. C. Nucleic Acid Delivery: The Missing Pieces of the Puzzle? *Acc. Chem. Res.* **45**, 1153–1162 (2012).

(35) Sahay, G.; Querbes, W.; Alabi, C.; Eltoukhy, A.; Sarkar, S.; Zurenko, C.; Karagiannis, E.; Love, K.; Chen, D.; Zoncu, R.; Buganim, Y.; Schroeder, A.; Langer, R.; Anderson, D. G. Efficiency of siRNA Delivery by Lipid Nanoparticles is Limited by Endocytic Recycling. *Nat. Biotechnol.* **31**, 653–658 (2013).

(36) Sahay, G.; Alakhova, D. Y.; Kabanov, A. V. Endocytosis of Nanomedicines. *J. Control. Release* **145**, 182–195 (2010).

(37) Luo, D.; Saltzman, W. M. Synthetic DNA Delivery Systems. *Nat. Biotechnol.* **18**, 33–37 (2000).

(38) Dykman, L. A.; Khlebtsov, N. G. Uptake of Engineered Gold Nanoparticles into Mammalian Cells. *Chem. Rev.* **114**, 1258–1288 (2013).

(39) Sharei, A.; Zoldan, J.; Adamo, A.; Sim, W. Y.; Cho, N.; Jackson, E.; Mao, S.; Schneider, S.; Han, M.-J.; Lytton-Jean, A.; Basto, P. A.; Jhunjhunwala, S.; Lee, J.; Heller, D. A.; Kang, J. W.; Hartoularos, G. C.; Kim, K.-S.; Anderson, D. G.; Langer, R.; Jensen, K. F. A Vector-Free Microfluidic Platform for Intracellular Delivery. *Proc. Natl. Acad. Sci. USA* **110**, 2082–2087 (2013).

(40) Whitehead, K. A.; Langer, R.; Anderson, D. G. Knocking Down Barriers: Advances in siRNA Delivery. *Nat. Rev. Drug Discov.* **8**, 129–138 (2009).

(41) Yeo, L. Y.; Friend, J. R. Surface Acoustic Wave Microfluidics. *Annu. Rev. Fluid Mech.* **46**, 379–406 (2014).

(42) Zeghimi, A.; Escoffre, J.; Bouakaz, A. Role of Endocytosis in Sonoporation-Mediated Membrane Permeabilization and Uptake of Small Molecules: A Electron Microscopy Study. *Phys. Biol.* **12**, 066007 (2015).

(43) Doudna, J. A.; Charpentier, E. The New Frontier of Genome Engineering with CRISPR-Cas9. *Science* **346**, 1258096 (2014).

(44) Demirci, U.; Montesano, G. Single Cell Epitaxy by Acoustic Picolitre Droplets. *Lab Chip* **7**, 1139–1145 (2007).

(45) Li, H.; Friend, J.; Yeo, L.; Dasvarma, A.; Traianedes, K. Effect of Surface Acoustic

Waves on the Viability, Proliferation and Differentiation of Primary Osteoblast-Like Cells. *Biomicrofluidics* **3**, 034102 (2009).

(46) Franke, T.; Braunmüller, S.; Schmid, L.; Wixforth, A.; Weitz, D. Surface Acoustic Wave Actuated Cell Sorting (SAWACS). *Lab Chip* **10**, 789–794 (2010).

(47) Nam, J.; Lim, H.; Kim, D.; Shin, S. Separation of Platelets From Whole Blood Using Standing Surface Acoustic Waves in a Microchannel. *Lab Chip* **11**, 3361–3364 (2011).

(48) Ding, X.; Lin, S.-C. S.; Kiraly, B.; Yue, H.; Li, S.; Chiang, I.-K.; Shi, J.; Benkovic, S. J.; Huang, T. J. On-Chip Manipulation of Single Microparticles, Cells, and Organisms Using Surface Acoustic Waves. *Proc. Natl. Acad. Sci. USA* **109**, 11105–11109 (2012).

(49) Collins, D. J.; Morahan, B.; Garcia-Bustos, J.; Doerig, C.; Plebanski, M.; Neild, A. Two-Dimensional Single-Cell Patterning with One Cell per Well Driven by Surface Acoustic Waves. *Nat. Commun.* **6**, 8686 (2015).

(50) Ren, L.; Chen, Y.; Li, P.; Mao, Z.; Huang, P.-H.; Rufo, J.; Guo, F.; Wang, L.; McCoy, J. P; Levine, S. J.; Huang, T. J. A High-Throughput Acoustic Cell Sorter. *Lab Chip* **15**, 3870–3879 (2015).

(51) Guo, F.; Li, P.; French, J. B.; Mao, Z.; Zhao, H.; Li, S.; Nama, N.; Fick, J. R.; Benkovic, S. J.; Huang, T. J. Controlling Cell–Cell Interactions Using Surface Acoustic Waves. *Proc. Natl. Acad. Sci. USA* **112**, 43–48 (2015).

(52) Guo, F.; Mao, Z.; Chen, Y.; Xie, Z.; Lata, J. P.; Li, P.; Ren, L.; Liu, J.; Yang, J.; Dao, M.; Suresh, S.; Huang, T. J. Thee-Dimensional Manipulation of Single Cells Using Surface Acoustic Waves. *Proc. Natl. Acad. Sci. USA* **113**, 1522–1527 (2016).

(53) Zhou, W.; Wang, J.; Wang, K.; Huang, B.; Niu, L.; Li, F.; Cai, F.; Chen, Y.; Liu, X.; Zhang, X.; Cheng, H.; Kang, L.; Meng, L.; Zheng, H. Ultrasound Neuro-Modulation

Chip: Activation of Sensory Neurons in *Caenorhabditis elegans* by Surface Acoustic Waves. *Lab Chip* **17**, 1725–1731 (2017).

(54) Qi, A.; Chan, P.; Ho, J.; Rajapaksa, A.; Friend, J.; Yeo, L. Template-Free Synthesis and Encapsulation Technique for Layer-by-Layer Polymer Nanocarrier Fabrication. *ACS Nano* **5**, 9583–9591 (2011).

(55) Rajapaksa, A. E.; Ho, J. J.; Qi, A.; Bischof, R.; Nguyen, T.-H.; Tate, M.; Piedrafita, D.; McIntosh, M. P.; Yeo, L. Y.; Meeusen, E.; Coppel, R. L.; Friend, J. R. Effective Pulmonary Delivery of an Aerosolized Plasmid DNA Vaccine via Surface Acoustic Wave Nebulization. *Respir. Res.* **15**, 60 (2014).

(56) Alhasan, L.; Qi, A.; Rezk, A. R.; Yeo, L. Y.; Chan, P. P. Y. Assessment of the Potential of a High Frequency Acoustomicrofluidic Nebulisation Platform for Inhaled Stem Cell Therapy. *Integr. Biol.* **8**, 12–20 (2016).

(57) Garibaldi, S.; Brunelli, C.; Bavastrello, V.; Ghigliotti, G.; Nicolini, C. Carbon Nanotube Biocompatibility with Cardiac Muscle Cells. *Nanotechnology* **17**, 391(2005).

(58) Pastan, I. H.; Willingham, M. C. Receptor-Mediated Endocytosis of Hormones in Cultured Cells. *Annu. Rev. Physiol.* **43**, 239–250 (1981).

(59) Liu, B. R.; Lo, S.-Y.; Liu, C.-C.; Chan, C.-L; Huang, Y.-W.; Aronstam, R. S.; Lee, H.-J. Endocytic Trafficking of Nanoparticles Delivered by Cell-Penetrating Peptides Comprised of Nona-Arginine and a Penetration Accelerating Sequence. *PLoS One* **8**, e67100 (2013).

(60) Yang, F.; Gu, N.; Chen, D.; Xi, X.; Zhang, D.; Li, Y.; Wu, J. Experimental Study on Cell Self-Sealing During Sonoporation. *J. Control. Release* **131**, 205–210 (2008).

(61) Zhao, Y.-Z.; Luo, Y.; Lu, C.-t.; Xu, J.-F.; Tang, J.; Zhang, M.; Zhang, Y.; Liang,

H.-D. Phospholipids-Based Microbubbles Sonoporation Pore Size and Reseal of Cell Membrane Cultured *In Vitro*. *J. Drug Target.* **16**, 18–25 (2008).

(62) Yoon, S.; Kim, M. G.; Chiu, C. T.; Hwang, J. Y.; Kim, H. H.; Wang, Y.; Shung, K. K. Direct and Sustained Intracellular Delivery of Exogenous Molecules Using Acoustic-Transfection with High Frequency Ultrasound. *Sci. Rep.* **6**, 20477 (2016).

(63) Kudo, N.; Okada, K.; Yamamoto, K. Sonoporation by Single-Shot Pulsed Ultrasound with Microbubbles Adjacent to Cells. *Biophys. J.* **96**, 4866–4876 (2009).

(64) Qi, A.; Friend, J. R.; Yeo, L. Y.; Morton, D. A.; McIntosh, M. P.; Spiccia, L. Miniature Inhalation Therapy Platform Using Surface Acoustic Wave Microfluidic Atomization. *Lab Chip* **9**, 2184–2193 (2009).

(65) Casal, H. L.; Mantsch, H. H. Polymorphic Phase Behaviour of Phospholipid Membranes Studied by Infrared Spectroscopy. *Biochim. Biophys. Acta. Rev. Biomembr.* **779**, 381–401 (1984).

(66) Szalontai, B.; Nishiyama, Y.; Gombos, Z.; Murata, N. Membrane Dynamics as Seen by Fourier Transform Infrared Spectroscopy in a Cyanobacterium, *Synechocystis* PCC 6803: The Effects of Lipid Unsaturation and the Protein-to-Lipid Ratio. *Biochim. Biophys. Acta. Rev. Biomembr.* **1509**, 409–419 (2000).

(67) Inaba, M.; Suzuki, I.; Szalontai, B.; Kanesaki, Y.; Los, D. A.; Hayashi, H.; Murata, N. Gene-Engineered Rigidification of Membrane Lipids Enhances the Cold Inducibility of Gene Expression in *Synechocystis*. *J. Biol. Chem.* **278**, 12191–12198 (2003).

(68) Los, D. A.; Murata, N. Membrane Fluidity and its Roles in the Perception of Environmental Signals. *Biochim. Biophys. Acta. Rev. Biomembr.* **1666**, 142–157 (2004).

(69) Zhou, Z.; Sun, X. X.; Ma, J.; Man, C. H.; Wong, A. S. T.; Leung, A. Y.; Ngan,

A. H. W. Mechanical Oscillations Enhance Gene delivery into Suspended Cells. *Sci. Rep.* **6**, 22824 (2016).

(70) Reusch, T.; Schülein, F. J. R.; Nicolas, J. D.; Osterhoff, M.; Beerlink, A.; Krenner, H. J.; Müller, M.; Wixforth, A.; Salditt, T. Collective Lipid Bilayer Dynamics Excited by Surface Acoustic Waves. *Phys. Rev. Lett.* **113**, 118102 (2014).

(71) Hodgson, R. P.; Tan, M.; Yeo, L.; Friend, J. Transmitting High Power rf Acoustic Radiation via Fluid Couplants into Superstrates for Microfluidics. *Appl. Phys. Lett.* **94**, 024102 (2009).

(72) Bourquin, Y.; Reboud, J.; Wilson, R.; Cooper, J. M. Tuneable Surface Acoustic Waves for Fluid and Particle Manipulations on Disposable Chips. *Lab Chip* **10**, 1898–1901 (2010).

(73) Vernekar, A. A.; Sinha,D.; Srivastava, S.; Paramasivam, P. U.; D'Silva, P.; Mugesh, G. An Antioxidant Nanozyme that Uncovers the Cytoprotective Potential of Vanadia Nanowires. *Nat. Commun.* **5**, 5301 (2014).

Acknowledgement

ARR is grateful for an RMIT University Vice-Chancellor's Postdoctoral Fellowship and LYY for an Australian Research Council (ARC) Future Fellowship (FT130100672). LYY also acknowledges funding from the ARC through Discovery Project (DP170101061). The authors thank Dr Zeyad Nasa for technical assistance with the use of the facilities at the RMIT MicroNano Research Facility.

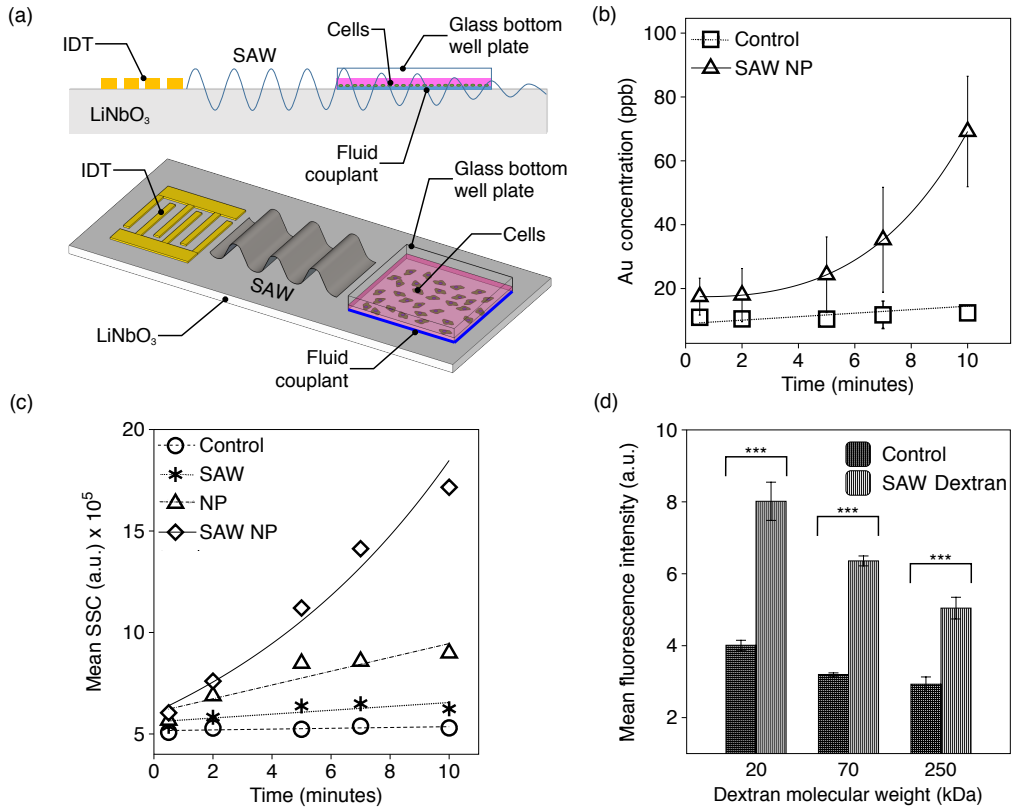

Figure 1: (a) Side (top) and perspective (bottom) view schematics of the experimental setup in which cells, cultured in a glass-bottom well plate, are exposed to the SAW irradiation (not to scale) generated when an AC electrical signal is applied to an interdigitated transducer (IDT) patterned on a piezoelectric ($LiNbO_3$) substrate and transmitted into the well plate via a fluid couplant (silicone oil). (b) Concentration of Au nanoparticles internalised in HEK293T cells at different time points, quantified using ICP-MS. (c) Flow cytometry side scatter, showing an increase in the Au nanoparticles internalised within the HEK293T cells in the presence of acoustic radiation (SAW NP), as a function of time; also shown are the cases where the cells were only exposed to the SAW for the same duration, but in the absence of the Au nanoparticles (SAW), and, in the presence of the Au nanoparticles but in the absence of SAW irradiation (NP), in which case the nanoparticles are passively internalised within the cell. (d) Mean fluorescence intensity of cells internalised with FITC-labelled dextrans of thee different molecular weights (20, 70 and 250 kDa), as analysed through flow cytometry. The data are represented in terms of the mean value ($n = 6$) $\pm$ the standard error. The asterisks *** indicate a statistically significant difference with $p < 0.001$.

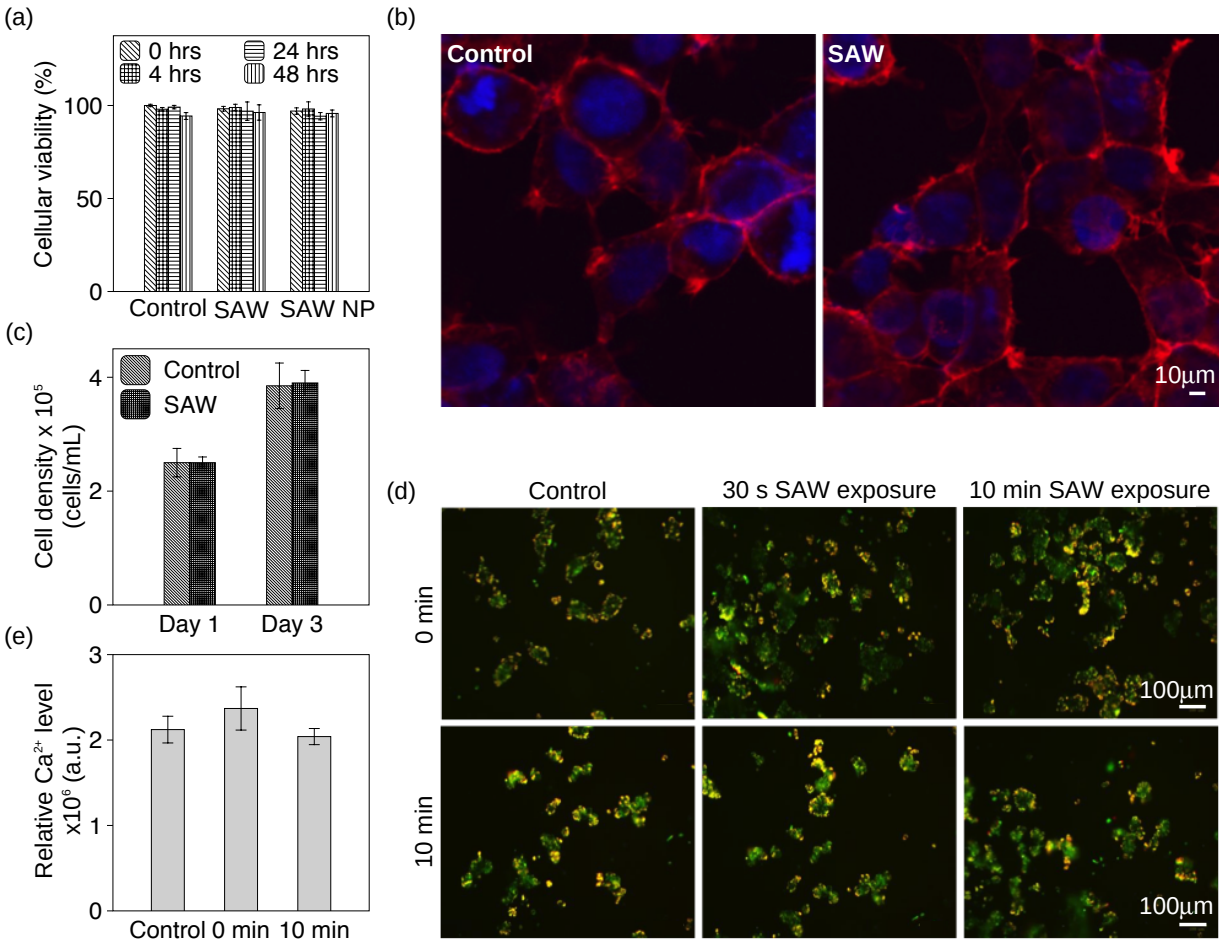

Figure 2: (a) Results from the MTT assay showing short and long term viability of HEK293T cells, immediately (0 min), 4 h, 24 h and 48 h after exposure to SAW irradiation over a 10 min duration, both in the absence (SAW) and in the presence (SAW NP) of the Au nanoparticles. (b) Confocal microscopy images of control (unexposed) cells and cells exposed to 10 mins of SAW irradiation. Actin filaments were stained by phalloidin (red) whereas the nuclei were stained by Hoechst 33342 (blue). (c) HEK293T cells exposed to 5 mins of SAW irradiation, showing an increase in the number of cells after re-seeding post SAW exposure. (d) Confocal microscopy images showing the mitochondrial membrane potential (MMP) via JC-1 dye staining of HEK293T cells that were exposed to 5 mins of SAW irradiation compared to the control. Regions of high mitochondrial polarisation are indicated by the red fluorescent aggregates whereas regions where the mitochondria have been depolarised are indicated by the green fluorescence emitted by the JC-1 monomers. (e) Calcium flux levels into HEK293T cells immediately and 10 mins after their exposure to 5 mins of SAW irradiation compared to the control, as observed using a Fura-2 acetoxymethyl ester (Fura-2 AM) assay. It can be seen that the flux levels into the cells temporarily increased immediately after cessation of the SAW irradiation but returned to comparable levels to that of the control within 10 mins.The data are represented in terms of the mean value ($n = 9$) $\pm$ the standard error.

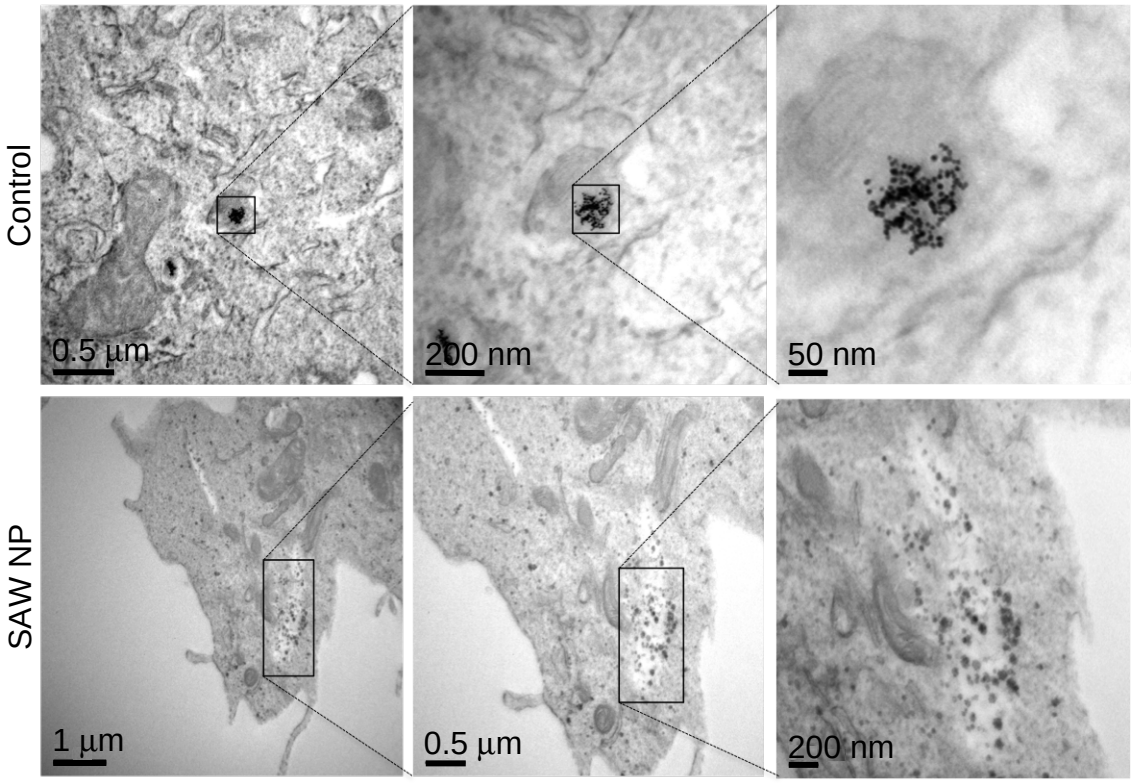

Figure 3: Representative TEM images showing the distribution of Au nanoparticles in HEK293T cells both in the presence (SAW NP) and absence of SAW exposure (control). The nanoparticles that were internalised passively in the control sample can be seen to be localised within endosomal organelles whereas the nanoparticles that were internalised via the acoustic excitation appear to be distributed throughout the cytosol.

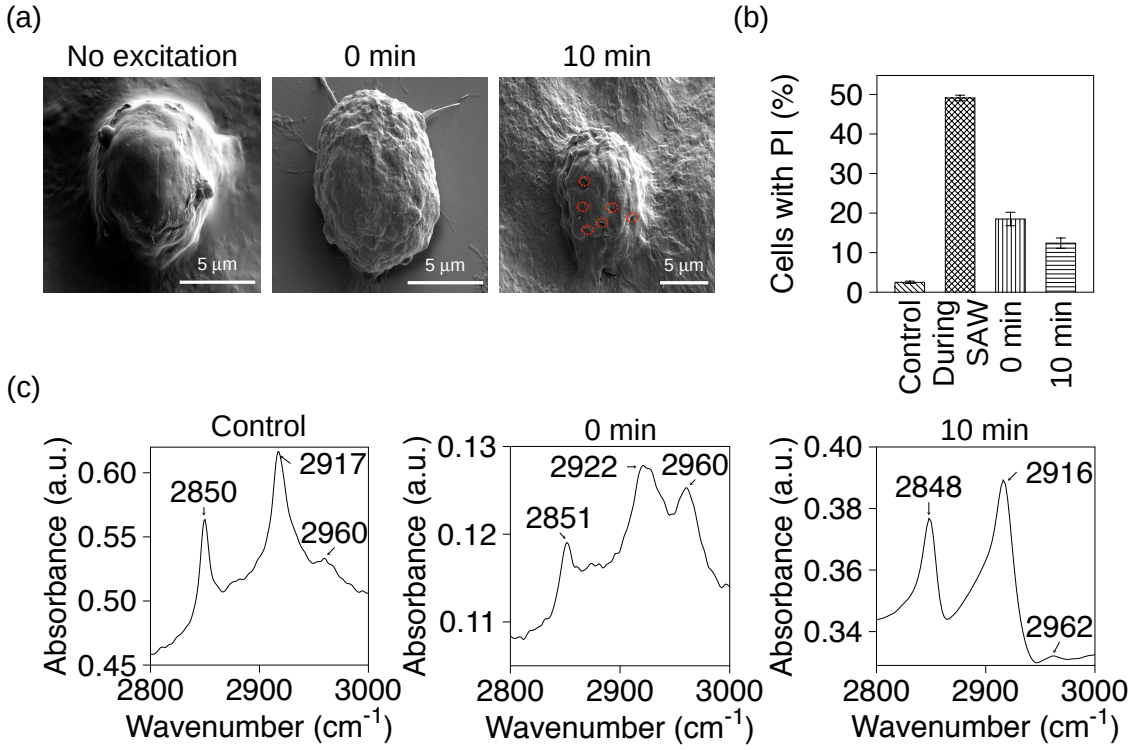

Figure 4: (a) SEM images showing the change in the surface morphology of a HEK293T cell fixed under 4% formaldehyde during exposure to SAW irradiation in the presence of Au nanoparticles (SAW NP) compared to that of an unexposed (control) cell. The red dashed circles indicate the existence of submicron surface aberrations in the irradiated sample, which, however, appear to be absent if the cells were not fixed, or if they were fixed immediately after relaxation of the SAW exposure (0 min). (b) The transient nature of the aberrations, and hence the propensity of the cells to rapidly self-heal can be seen through the addition of propidium iodide (PI) to the cells, whose internalisation is an indicator of cell membrane permeability. The increase of PI intake within the cells during exposure to the SAW for 10 mins then indicates a degree of membrane permeabilisation compared to the unexposed control, whereas the immediate decrease in the intake immediately upon (0 min) and 10 mins after removal of the acoustic excitation suggests its transient nature. Error bars denote the mean value ± the standard error. (c) FTIR absorption spectra supporting the possibility of lipid reorganisation within the cell membrane during SAW irradiation. The respective absorption bands at 2851 cm^{-1} and 2917 cm^{-1} are related to the symmetric and anti-symmetric vibrational stretching of the CH_2 groups in the lipids that make up the cell membrane, whereas that at 2960 cm^{-1} corresponds to the anti-symmetric vibrational stretching of the CH_3 group. A frequency shift in these bands, as seen by the spectra for the cells collected immediately (0 min) upon relaxation of the SAW excitation compared to the control, indicates a change in the lipid conformation as a consequence of the acoustic irradiation. It can be seen that this lipid reorganisation is however transient in nature given that the absorption band reverts to its near original frequency 10 mins after the exposure.

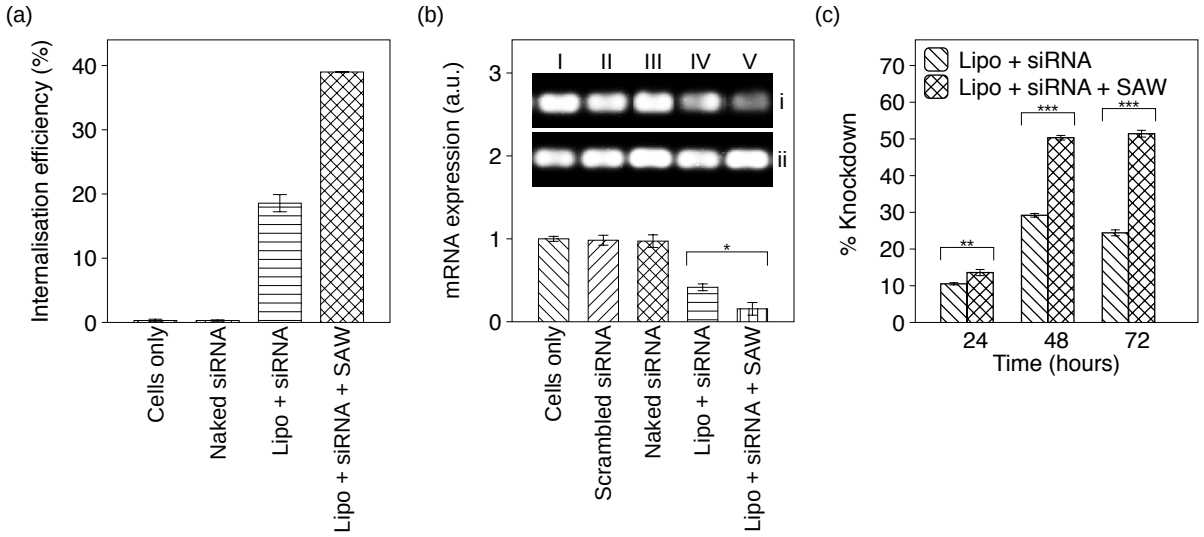

Figure 5: (a) Internalisation efficiency of Cy3-labelled GAPDH siRNA in HeLa cells from measurements of the fluorescence intensity using flow cytometry. The data in the first two columns represent the mock and negative controls comprising cells alone without the siRNA, or with naked siRNA in the absence of the transfection agent Lipofectamine®. The data in the following two columns comprises that for cells in the presence of both siRNA and Lipofectamine® when they are unexposed and exposed to SAW irradiation over a duration of 5 mins. (b) GAPDH mRNA expression, measured by qRT-PCR and gel electrophoresis end point analysis of the amplified DNA (inset). Similar to the qPCR results, the lanes represent the mock and sham (scrambled siRNA) controls, naked siRNA, siRNA and Lipofectamine® unexposed to the SAW, and, siRNA in the presence of Lipofectamine® and the SAW, respectively. The first row of the gel bands (i) represents the GAPDH levels whereas the second row (ii) represents the β-actin reference gene levels that were measured. (c) GAPDH protein knockdown at various timepoints after exposure of the cells to the SAW. The data are represented in terms of a mean value ($n = 23$) $\pm$ the standard error. The asterisks *, ** and *** indicate statistically significant differences with $p < 0.1$, $p < 0.01$ and $p < 0.001$, respectively.

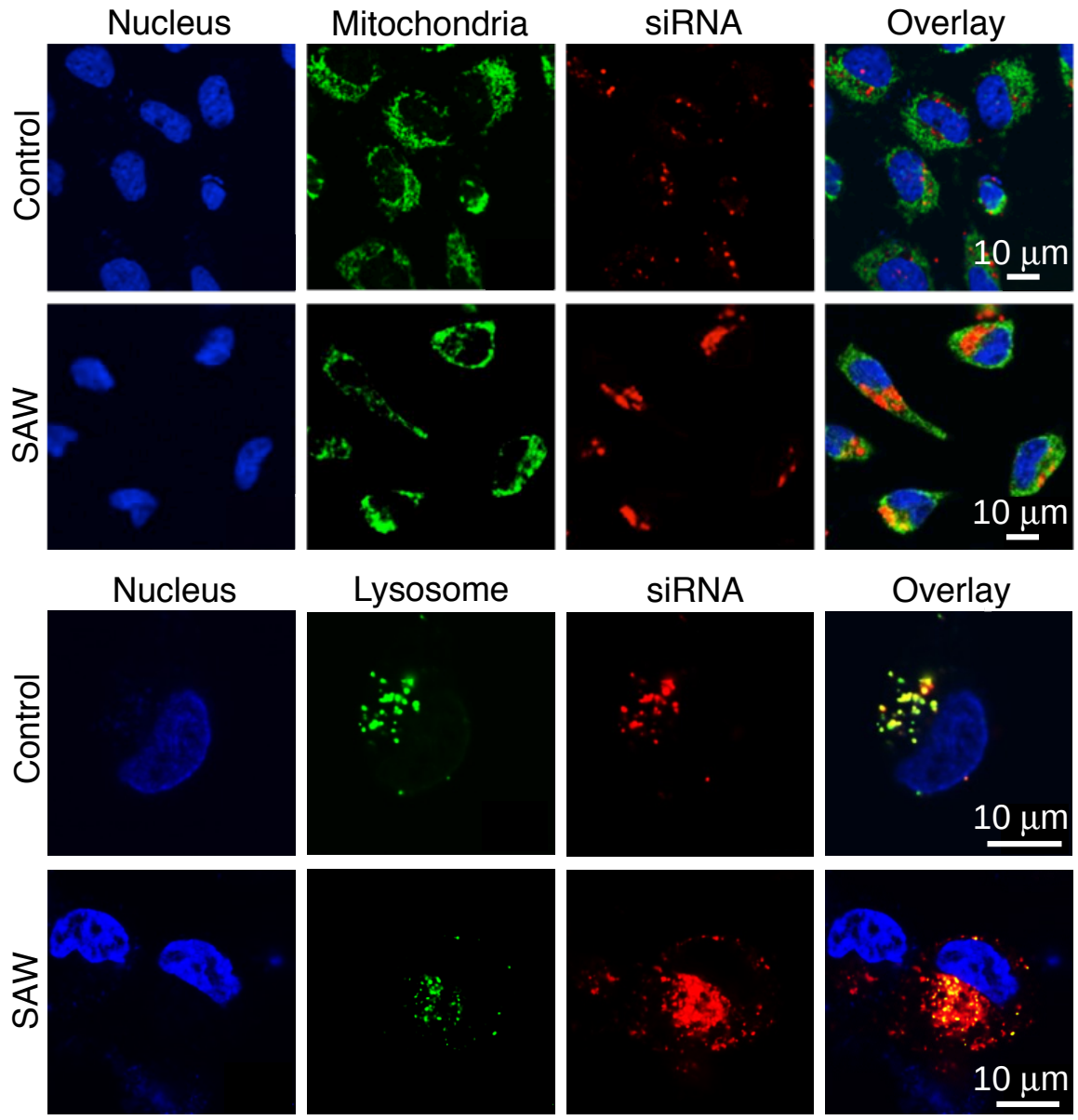

Figure 6: Representative confocal microscopy images showing the distribution of Cy3-labelled GAPDH siRNA in HeLa cells when they are passively internalised in the control experiment (no SAW exposure) and when they are internalised under the influence of 5 min of SAW excitation in the presence of Lipofectamine®. The cell nuclei were stained by Hoechst 33342 (blue) in all the images. The mitochondria in the top two rows were stained using MitoTracker® Green whereas lysosomes in the bottom two rows were stained using LysoTracker® Green. The overlay in the last column thus comprised a merger of the individual channels showing co-localisation of the siRNA within the endosomal compartments for the unexposed samples, whereas the siRNA appears to be distributed throughout the cytosol for samples that have been irradiated with the SAW.